

Intelligent Image De-Blurring for Imaging Flow Cytometry

Fangzheng Zhang,^{1,2} Cheng Lei,^{1,3*} Chun-Jung Huang,^{1,4} Hirofumi Kobayashi,¹ Chia-Wei Sun,⁴ Keisuke Goda^{1,3,5}

¹Department of Chemistry, University of Tokyo, Tokyo, Japan

²College of Electronic and Information Engineering, Nanjing University of Aeronautics and Astronautics, Nanjing, 211106, China

³Institute of Technological Sciences, Wuhan University, Wuhan, 430072, China

⁴Department of Photonics, College of Electrical and Computer Engineering, National Chiao Tung University, Hsinchu, Taiwan

⁵Japan Science and Technology Agency, Kawaguchi, Japan

Received 18 January 2019; Revised 19 March 2019; Accepted 1 April 2019

Grant sponsor: China Scholarship Council; Grant sponsor: Cabinet Office, Government of Japan; Grant sponsor: JSPS Core-to-Core Program

*Correspondence to: Cheng Lei, Department of Chemistry, University of Tokyo, Tokyo, Japan. Email: leicheng@chem.s.u-tokyo.ac.jp

Published online in Wiley Online Library (wileyonlinelibrary.com)

DOI: 10.1002/cyto.a.23771

© 2019 International Society for Advancement of Cytometry

• Abstract

By virtue of the combined merits of optical microscopy and flow cytometry, imaging flow cytometry is a powerful tool for rapid, high-content analysis of single cells in large heterogeneous populations. However, its efficiency (defined by the ratio of the number of clearly imaged cells to the total cell population) is not high (typically 50–80%), due to out-of-focus image blurring caused by imperfect fluidic focusing of cells, a common drawback that not only reduces the number of cell images useable for high-content analysis but also increases the probability of false events and missed rare cells. To address this challenge and expand the efficacy of imaging flow cytometry, here, we propose and demonstrate intelligent deblurring of out-of-focus cell images in imaging flow cytometry. Specifically, by using our machine learning algorithms, we show an 11% increase in variance and a 95% increase in first-order gradient summation of cell images taken with an optofluidic time-stretch microscope. Without strict hardware requirements, our intelligent de-blurring method provides a promising solution to the out-of-focus blurring problem of imaging flow cytometers and holds promise for significantly improving their performance. © 2019 International Society for Advancement of Cytometry

• Key terms

Imaging flow cytometry; image de-blurring; machine learning; optofluidic time-stretch microscopy

WITH the combined merits of optical microscopy and flow cytometry, imaging flow cytometry has become an established tool for rapid, high-content analysis of single cells in large heterogeneous populations (1–9). It has found a wide range of applications in microbiology, stem cell biology, immunology, and marine biology (3,10,11). Imaging flow cytometry provides quantitative image data of every event, allowing for the morphometric assessment of single cells and further advancing our understanding of the vast heterogeneity of cells (12). The availability of image data produced by an imaging flow cytometer is aligned with the pressing need for progressively larger biomedical datasets for efficient and accurate data analysis to make better decisions in biomedical research and clinical settings (13). According to recent reports (14,15), imaging flow cytometry has been shown to be highly effective for the accurate evaluation of cell death and autophagy, fluorescence in situ hybridization (FISH), the localization and enumeration of transcription factors, the characterization of DNA damage and repair, and the analysis of cell–cell interactions. In addition to applications for basic research, imaging flow cytometry has also found clinical utility for applications such as liquid biopsy and infectious disease detection (16,17). By virtue of these numerous capabilities and applications, imaging flow cytometry is expected to grow in the next decade.

Unfortunately, imaging flow cytometry suffers from out-of-focus image blurring caused by imperfect fluidic focusing of cells, resulting in an efficiency (defined by the ratio of the number of clearly imaged cells to the total cell population) of 50–80%, meaning that 20–50% of cells in the flow are not properly imaged (3). The

focusing problem is attributed to cell-to-cell fluctuations in position at the moment when the flowing cell passes through the imaging area in a capillary tube or microchannel (18). This makes it difficult to see the detailed structure of cells, even if the spatial resolution of the imaging flow cytometer is high, significantly reducing the effective number of cell images for high-content analysis and increasing the chance of false events and missed rare cells. Several fluidic focusing techniques, such as hydrodynamic focusing (19), inertial focusing (18), and acoustic focusing (20), can be used to introduce external forces for confining cells in a specific focal plane, but the heterogeneous nature of cells (i.e., non-uniform cell size, shape, mass, density, stiffness) limits the effectiveness of these techniques, making it infeasible to reach perfect cell focusing and an efficiency of 100%. While digital image de-blurring techniques have been demonstrated for macroscopic images or videos by applying specific de-blurring filters (21) or machine learning (22) to them, these methods have not been demonstrated on microscopic images yet.

In this article, we propose and demonstrate intelligent de-blurring of out-of-focus cell images in order to improve the efficiency of an imaging flow cytometer. Specifically, with our technique, we establish and optimize a two-stage machine-learning network with a residual network (ResNet) structure and then feed blurred cell images to the optimized machine-learning network to de-blur them. To investigate the performance of this method, we used an optofluidic time-stretch microscope as a bright-field imaging flow cytometer to acquire both blurred and unblurred images of K-562 cells (human immortalized myelogenous leukemia cell line), applied intelligent de-blurring to them, and significantly improved the visibility of the detailed structure of the cells in the blurred cell images. Quantitatively, the variance and the first-order gradient summation of the blurred images, which are commonly used parameters to evaluate the quality of images, were increased by 11% and 95%, respectively. Our intelligent de-blurring method provides a promising solution to the cellular out-of-focus blurring problem, without strict hardware requirements for imaging flow cytometers.

METHODS

Figure 1 shows a typical imaging flow cytometry system consisting of an optical microscope and a capillary tube or a microchannel. The microscope performs high-resolution

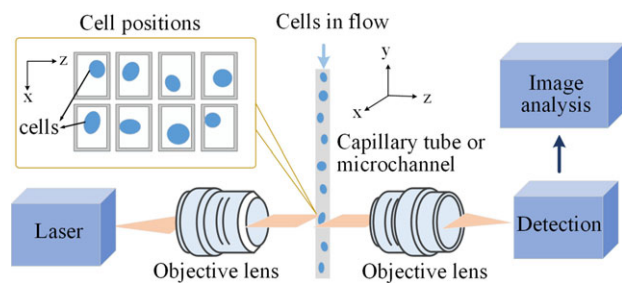


Figure 1. Schematic diagram of a typical imaging flow cytometry system. Out-of-focus image blurring occurs due to imperfect fluidic focusing of cells in a capillary tube or microfluidic channel.

imaging of cells that pass through the capillary tube or microchannel. The incident light of the microscope is focused on the imaging area within the capillary tube or microchannel through an objective lens. To obtain clear images, the cells should flow exactly in the focal plane of the objective lens. Since the size of the capillary tube or microchannel is usually larger than that of the cells, they flow in different planes when passing through the imaging area, as illustrated in the inset of Figure 1. Even if cell focusing techniques are applied, the cells still flow in different planes inside the capillary tube or microchannel due to their heterogeneous nature (i.e., non-uniform cell size, shape, mass, density, stiffness). When cells deviate from the focal plane of the objective lens, the obtained images are blurred.

To deal with this problem, our method for de-blurring out-of-focus cell images was achieved by applying machine learning without the need for extraordinary hardware. Figure 2 shows the structure of the machine-learning network that we employed for intelligent image de-blurring. Since it is impractical to acquire both blurred and unblurred images of the same cells to train the network, we selected unblurred images obtained by the imaging flow cytometer and blurred them by low-pass filtering to simulate the image-blurring effects due to the out-of-focus problem (23). The artificially blurred images were used as the input of the network while the corresponding unblurred images were used as the targets to train the network. The machine-learning network in Figure 2 includes two stages. The first stage is composed of several processing blocks, each of which consists of a 2D convolutional layer followed by a rectified linear unit (ReLU) as the activation function (24). To allow for high-level feature inference, the numbers of features learnt in the processing blocks are first increased by gradually increasing the number of output channels in each 2D convolutional layer, for example, from 1 to M , and then decreased by gradually reducing the number of output channels from M to 1. This way, the output images of the first stage have the same size as the input images. The second stage has the same structure as the first stage, but there is a shortcut connection between the input and output. This residual network (ResNet) configuration is helpful to achieve good training performance and a rapid convergence (25). The output images from the second stage are compared with the unblurred images to calculate the errors. The loss function is defined as the weighted superposition of the mean square error (MSE) and the first-order gradient difference between the output images and the unblurred images, which considers both the similarity and sharpness of the images (24). The errors calculated with the loss function are backpropagated through the network while the network's parameters are updated using the adaptive moment estimation (ADAM) optimization (26). Once the network is optimized and validated, image de-blurring is performed by simply feeding the blurred images to the network.

To investigate the performance of the intelligent image de-blurring method, an optofluidic time-stretch microscope was used as an imaging flow cytometer to acquire both blurred and unblurred images of K-562 cells (a leukemia cell line). Figure 3 shows a schematic diagram of the optofluidic time-stretch

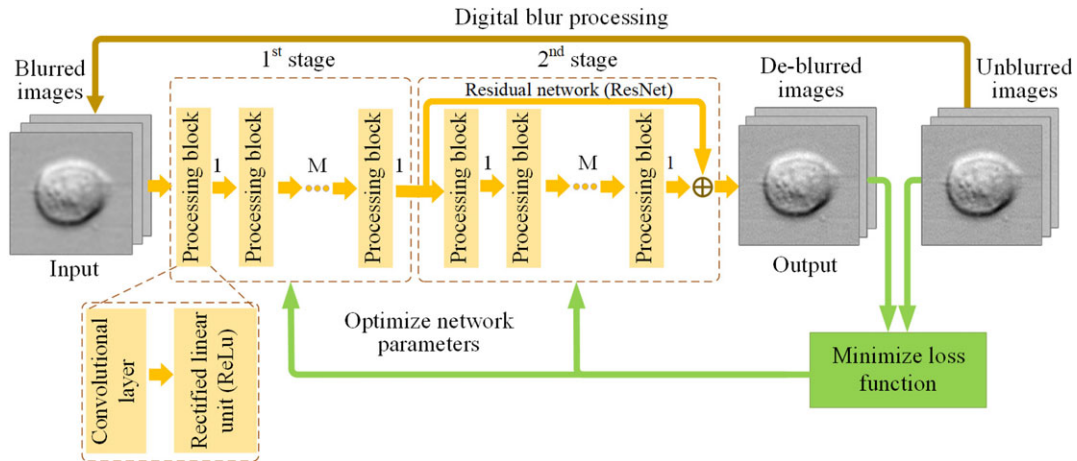


Figure 2. Structure of the machine-learning network used for intelligent image de-blurring of out-of-focus cell images. The network includes two stages. The output images from the second stage are compared with the unblurred images to calculate errors or differences between the unblurred and de-blurred images. The errors calculated with the loss function are backpropagated through the network while the network's parameters are updated using the ADAM optimization.

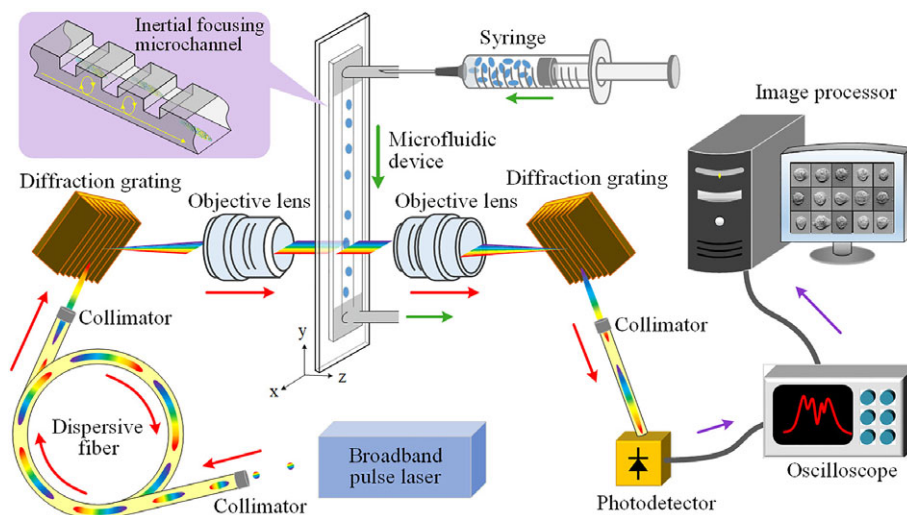


Figure 3. Schematic diagram of the optofluidic time-stretch microscope for demonstrating intelligent image de-blurring of out-of-focus cell images.

microscope, which is mainly composed of a broadband pulse laser (Spectra Physics Tsunami 3941-50NS-UPG-FE and Millennia EV 10-TG-FE, center wavelength 790 nm, bandwidth 40 nm, repetition rate 75 MHz), a temporal disperser (Nufern 630-HP, total amount of dispersion is -240 ps/nm), a spatial disperser (a pair of diffraction gratings with a groove density of 1,200 lines/mm), a pair of objective lenses (Olympus LUCPlanFLN 40 \times , NA 0.6), a microfluidic device (home-made hydrodynamic-focusing microchannel), a single-pixel photodetector (New Focus 1,580-B, bandwidth 12 GHz), a digitizer (Tektronix DPO71604B, sampling rate 50 GS/s, bandwidth 16 GHz), and a digital signal processor. The optical pulse from the broadband pulse laser is first sent to the dispersive fiber, where the pulse is stretched in the time domain. Then, the stretched pulse is spatially dispersed by the first diffraction

grating. Thus, different frequency components of the pulse are diffracted at different angles, resulting in a 1D rainbow-like profile. After that, this 1D rainbow pulse is focused onto the microfluidic device by the first objective lens. Different coordinates on the target are illuminated by different frequency components of the pulse. Therefore, the spatial information of the target is encoded in the spectrum of the pulse. Next, the encoded pulse is collected and recombined by the second objective lens and the second diffraction grating. Finally, the pulse is detected and digitized by the single-pixel photodetector and the digitizer, respectively. In this process, each pulse takes one cross section of the target. By digitally stacking multiple pulses, 2D images of the targets can be constructed.

Figure 4 shows typical unblurred and blurred images of K562 cells, where the unblurred images have obviously higher

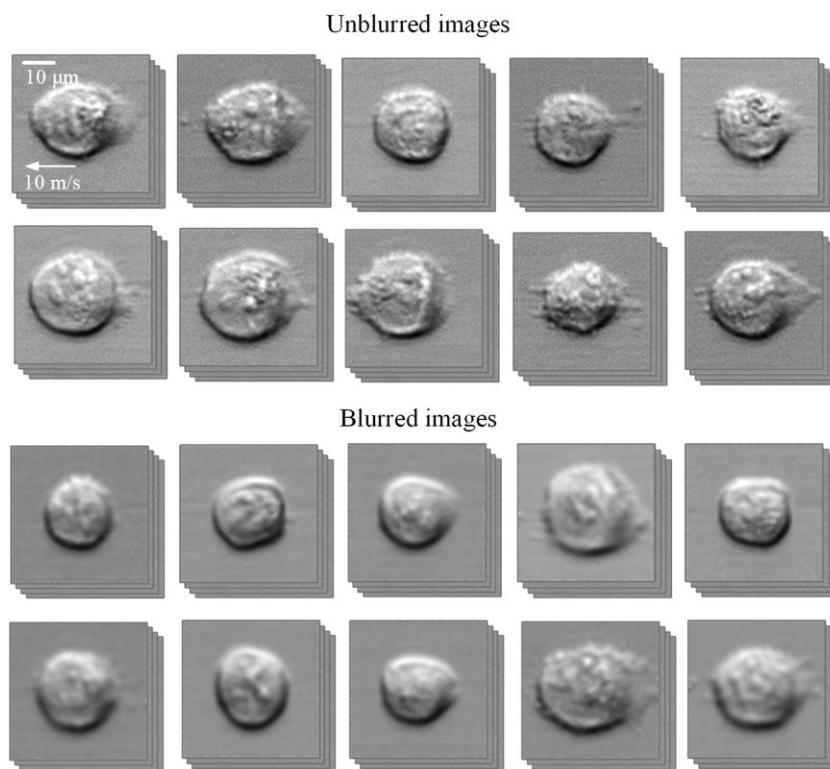


Figure 4. Unblurred and blurred images of K-562 cells captured by an optofluidic time-stretch microscope.

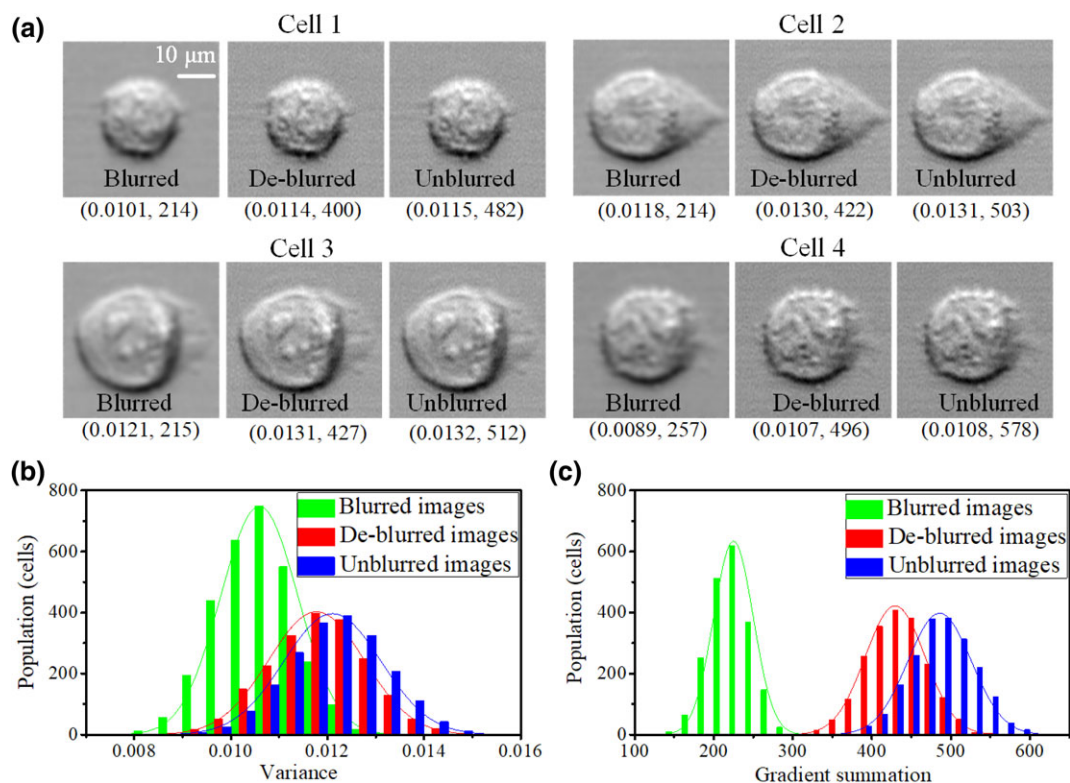


Figure 5. Performance of the machine-learning-based image de-blurring network. (a) Blurred images, de-blurred images and unblurred images of four K562 cells. (b) Histograms of variance of 2,000 cell images. (c) Histogram of 2,000 cell images in gradient summation.

clarity and higher contrast compared to the blurred ones. The fine structures of the cells are evident in the unblurred images, while the details of the cells can hardly be discerned in the blurred images. In this experiment, 11,000 unblurred images of the K-562 cells were obtained, of which 9,000 images were used to train the machine-learning network while the remaining 2,000 images were used for validating the trained network. Before training and validating the network, the amplitudes of all the images were normalized to a range of 0–1. The machine-learning network was established in a Python (version 3.6) environment using Keras as the application programming interface (API). The images of the training set were first blurred by an image-blurring filter with a 5×5 kernel and then fed to the input of the network. In each stage of the network, there were nine processing blocks, of which the output numbers of channels were 1, 4, 8, 16, 32, 64, 16, 4, and 1, respectively. All the kernels used in the convolutional layers had 3×3 elements and all the bias terms were initialized to 0. To avoid over-fitting when training the network, early stopping was applied in the training process.

RESULTS

After training the network, its performance was tested using the validation set composed of 2,000 unblurred and corresponding artificially blurred image pairs. Figure 5a shows the blurred images, de-blurred images, and unblurred images of four K562 cells, where the de-blurred images have apparently higher clarity than that of the blurred images and similar quality as the unblurred images. To quantitatively show the

improvement of image quality, the variance and the first-order gradient summation of the images were calculated (27,28). In Figure 5a, the first values in the brackets below each image are the variances of the images, whereas the second values are the first-order gradient summations. For cell 1, after de-blurring, the values of the two parameters increased from (0.0101, 214) to (0.0114, 400) close to those of the unblurred image with (0.0115, 482). Here, the increase in the variance and gradient summation indicates the image contrast is dramatically enhanced after de-blurring. For cells 2, 3, and 4, the variance and first-order gradient summation also notably increased after de-blurring. Figure 5b shows histograms of the images of all 2,000 K562 cells in the variance, in which the average variance of the blurred images, de-blurred images, and unblurred images were found to be 0.0106, 0.0119, and 0.0121, respectively. Figure 5c shows histograms of the images of the 2,000 K562 cells in the gradient summation, where the average values are 225, 430, and 486, for the blurred images, de-blurred images, and unblurred images, respectively. These results quantitatively verify that the optimized machine-learning network achieved effective image de-blurring.

Finally, to validate the performance of our method in practice, de-blurring of blurred images (obtained by the optofluidic time-stretch microscope) was performed by feeding them to the optimized machine-learning network. Figure 6a shows the blurred images and de-blurred images of three K562 cells, where the de-blurred images have obviously higher clarity than that of the blurred images. In the enlarged views of certain areas of each image in Figure 6a, fine cell structures that cannot be distinguished in the blurred images became clear in

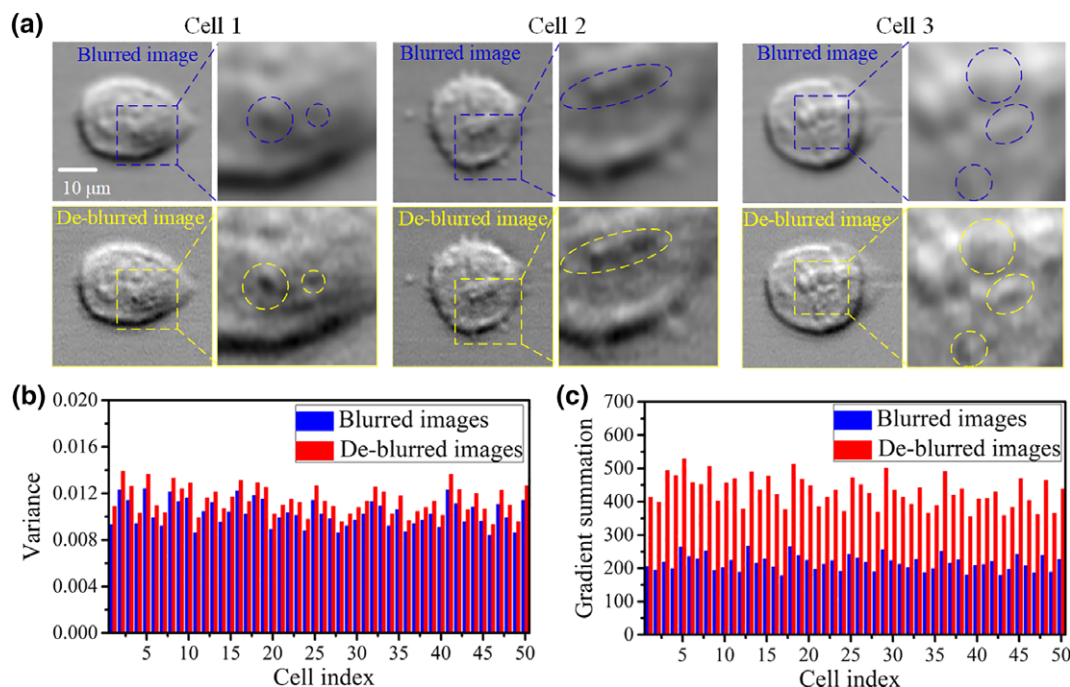


Figure 6. De-blurring performance of the blurred images captured by the optofluidic time-stretch microscope. (a) Blurred images and de-blurred images of three K562 cells. (b) Comparison of 50 cell images in variance. (c) Comparison of 50 cell images in gradient summation.

the de-blurred images, indicating that the image quality was significantly improved. To statistically show the improvement, the blurred and de-blurred images of 50 K562 cells were compared in terms of the variance and gradient summation, as shown in Figure 6b,c. In general, both the variance and gradient summation increased after de-blurring by the optimized machine-learning network. On average, the variance of an image increased by 11%, while the gradient summation increased by 95%. These results firmly show that the optimized machine-learning network is capable of remarkably improving the quality of blurred images acquired with the optofluidic time-stretch microscope.

DISCUSSION

There are a few points to discuss regarding the proposed image de-blurring method. First, although the method was experimentally validated on the optofluidic time-stretch microscopy platform with K562 cells, it is also applicable to imaging flow cytometry based on other imaging modalities, such as bright-field imaging with CCD/CMOS image sensors, fluorescence imaging, and quantitative phase imaging as well as other cell types. Second, the structure of the network (such as the number of layers, stages, as well as the number of output channels in each layer) may be different in different applications. Since the images obtained by the optofluidic time-stretch microscope are simply in grayscale and have many similar structures, a two-stage network was sufficient for our demonstration. For colorful or other complicated images, more stages are preferred to achieve a high image de-blurring performance. As for the parameters in each stage of the network, we found that a larger number of layers, a larger number of output channels, or a smaller changing step of the output channel between adjacent layers led to a high-level feature interaction between different images, and hence helped achieve a higher de-blurring performance. However, this also means that the computational complexity is increased, leading to requirements for more computational resources (e.g., time, hardware, electrical power). Thus, there exists a trade-off between the performance and computational complexity. We believe this intelligent image de-blurring method is a promising solution to the cellular out-of-focus blurring problem, without strict hardware requirements, for imaging flow cytometers.

ACKNOWLEDGMENTS

This work was primarily funded by the ImPACT Program of the CSTI (Cabinet Office, Government of Japan) and partly by the JSPS Core-to-Core Program. F. Z. was supported by the China Scholarship Council (CSC).

CONFLICT OF INTERESTS

The authors declare that they have no conflicts of interests.

LITERATURE CITED

- Nitta N, Sugimura T, Isozaki A, Mikami H, Hiraki K, Sakuma S, Ino T, Arai F, Endo T, Fujiwaki Y, et al. Intelligent image-activated cell sorting. *Cell* 2018;175:266–276.
- Goda K, Ayazi A, Gossett DR, Sadasivam J, Lonappan CK, Sollier E, Fard AM, Hur SC, Adam J, Murray C, et al. High-throughput single-microparticle imaging flow analyzer. *Proc Natl Acad Sci* 2012;109:11630–11635.
- Lei C, Kobayashi H, Wu Y, Li M, Isozaki A, Yasumoto A, Mikami H, Ito T, Nitta N, Sugimura T, et al. High-throughput imaging flow cytometry by optofluidic time-stretch microscopy. *Nat Protoc* 2018;13:1603–1631.
- Lei C, Guo B, Cheng Z, Goda K. Optical time-stretch imaging: Principles and applications. *Appl Phys Rev* 2016;3:011102.
- Mikami H, Lei C, Nitta N, Sugimura T, Ito T, Ozeki Y, Goda K. High-speed imaging meets single-cell analysis. *Chem* 2018;4:2278–2300.
- Mikami H, Harmon J, Kobayashi H, Hamad S, Wang Y, Iwata O, Suzuki K, Ito T, Aisaka Y, Kutsuna N, et al. Ultrafast confocal fluorescence microscopy beyond the fluorescence lifetime limit. *Optica* 2018;5:117–126.
- Han Y, Gu Y, Zhang AC, Lo YH. Review: Imaging technologies for flow cytometry. *Lab Chip* 2016;16:4639–4647.
- Basiji D, O’Gorman MR. Imaging flow cytometry. *J Immunol Methods* 2015;423:1–2.
- Porichis F, Hart MG, Griesbeck M, Everett HL, Hassan M, Baxter AE, Lindqvist M, Miller SM, Soghoian DZ, Kavanagh DG, et al. High-throughput detection of miRNAs and gene-specific mRNA at the single-cell level by flow cytometry. *Nat Commun* 2014;5:5641.
- Rodrigues MA, Beaton-Green LA, Wilkins RC, Fenech MF. The potential for complete automated scoring of the cytokinesis block micronucleus cytome assay using imaging flow cytometry. *Mutat Res-Gen Tox En* 2018;836:53–64.
- Lai QTK, Lee KCM, Tang AHL, Wong KKY, So HKH, Tsia KK. High-throughput time-stretch imaging flow cytometry for multi-class classification of phytoplankton. *Opt Express* 2016;24:28170–28184.
- Rane AS, Rutkauskaitė J, deMello A, Stavrakis S. High-throughput multi-parametric imaging flow cytometry. *Chem* 2017;3:588–602.
- Doan M, Vorobjev I, Rees P, Filby A, Wolkenhauer O, Goldfeld AE, Lieberman J, Barteneva N, Carpenter AE, Hennig H. Diagnostic potential of imaging flow cytometry. *Trends Biotechnol* 2018;36:649–652.
- Fashauer M, Kruwel T, Zapf A, Stahnke VC, Rave-Fränk M, Staab W, Sohns JM, Steinmetz M, Unterberg-Buchwald C, Schuster A, et al. Absence of DNA double-strand breaks in human peripheral blood mononuclear cells after 3 Tesla magnetic resonance imaging assessed by gamma H2AX flow cytometry. *Eur Radiol* 2018;28:1149–1156.
- Hritzó MK, Courneya JP, Golding A. Imaging flow cytometry: A method for examining dynamic native FOXO1 localization in human lymphocytes. *J Immunol Methods* 2018;454:59–70.
- Alix-Panabieres C, Pantel K. Circulating tumor cells: Liquid biopsy of cancer. *Clin Chem* 2013;59:110–118.
- Haridas V, Ranjbar S, Vorobjev IA, Goldfeld AE, Barteneva NS. Imaging flow cytometry analysis of intracellular pathogens. *Methods* 2017;112:91–104.
- Di Carlo D, Irimia D, Tompkins RG, Toner M. Continuous inertial focusing, ordering, and separation of particles in microchannels. *Proc Natl Acad Sci* 2007;104:18892–18897.
- Hung CI, Ke BJ, Huang GR, Hwei BH, Lai HF, Lee GB. Hydrodynamic focusing for a micromachined flow cytometer. *J Fluid Eng-T ASME* 2001;123:672–679.
- Piyasena ME, Suthanthiraraj PPA, Applegate RW, Goumas AM, Woods TA, López GP, Graves SW. Multinode acoustic focusing for parallel flow cytometry. *Anal Chem* 2012;84:1831–1839.
- Gong W, Wang W, Li W, Shu T. Temporal consistency based method for blind video deblurring. *Proceedings of the International Conference on Pattern Recognition, Stockholm, Sweden; 2014*. pp. 861–864.
- Zhe H, Huang J B, Yang M H. Single image deblurring with adaptive dictionary learning. *Proceedings of the IEEE International Conference on Image Process, Hong Kong, China; 2010*. pp. 1169–1172.
- Sezan MI, Pavlovic G, Tekalp AM, Erdem AT. On modeling the focus blur in image-restoration. *Proceedings of the International Conference on Acoust Speech Signal Process, Toronto, Canada; 1991*. pp. 2485–2488.
- He KM, Zhang XY, Ren SQ, Sun J. Deep residual learning for image recognition. *Proceedings of the IEEE Conference on Computer Vision Pattern Recognition, Seattle, USA; 2016*. pp. 770–778.
- Rivenson Y, Göröcs Z, Günaydin H, Zhang Y, Wang H, Ozcan A. Deep learning microscopy. *Optica* 2017;4:1437–1443.
- Kingma DP, Ba J. Adam: A method for stochastic optimization. *arXiv* 2017;1412.6980v1419.
- Eskicioglu AM, Fisher PS. Image quality measures and their performance. *IEEE Trans Commun* 1995;43:2959–2965.
- Liu LX, Hua Y, Zhao QJ, Huang H, Bovik AC. Blind image quality assessment by relative gradient statistics and adaboosting neural network. *Signal Process Image Commun* 2016;40:1–15.